Capabilities of DIMAXER in predicting slat noise from high-lift systems

Keli Zhang*, Peiqing Liu*, Shizhi Lin*, Shihao Liu¶, Yuping Ren†, Can Fang†, Aiqi Zhu‡, Kai Liu‡, Yi Lu§ and Yu Lv‖
Corresponding author: lpq@buaa.edu.cn
* School of Aeronautic Science and Engineering, Beihang University, Beijing, 100191, PR China.
¶ Department of Mathematics, Linné FLOW Centre, KTH Royal Institute of Technology, 100 44, Stockholm, Sweden.
† Rankyee Technology Suzhou, Suzhou 215128, PR China.
‡ Rankyee Technology Beijing, Beijing 100036, PR China.
§ Rankyee Technology Shenzhen, Shenzhen 518038, PR China.
‖ State Key Laboratory of Nonlinear Mechanics, Institute of Mechanics, Chinese Academy of Sciences, Beijing 100190, PR China.

Abstract: Wall-resolved large-eddy simulation (WRLES) has traditionally been considered computationally prohibitive for engineering applications. This study demonstrates affordable aeroacoustic prediction of high-lift device slat noise using high-order WRLES coupled with the Ffowcs Williams-Hawkings (FW-H) acoustic analogy. The space-time expansion of high-order kinetic preserving flux reconstruction scheme (STE-KEP-FR) enables efficient computation, with only a few GPUs required to perform WRLES simulations. Two high Reynolds number benchmarks are examined: the 30P30N high-lift airfoil and the Trap Wing semi-span model. These configurations represent 2.5D and 3D slat noise problems with degrees of freedom (DoFs) ranging from 31.3 million to 0.32 billion. Results demonstrate excellent agreement with experimental data. The 30P30N benchmark case demonstrates that our high-order solver DIMAXER achieves two orders of magnitude higher accuracy and computational efficiency compared to the CPU-based second-order finite volume solver OpenCFD-EC.

Keywords: Aeroacoustics, High-order, Flux Reconstruction, LES, High-lift Systems.

1. Introduction

Accurate aeroacoustic prediction first requires high-fidelity unsteady flow field simulation. Previous research has indicated that for engineering-level aviation acoustic problems with peak and broadband noise, at least a hybrid Reynolds-averaged Navier-Stokes (RANS)/large-eddy simulation (LES) flow field is necessary. Subsequently, coupling the unsteady flow field result with the Ffowcs Williams-Hawkings (FW-H) acoustic analogy [1] to calculate far-field noise is a common practice in the field of computational aeroacoustics (CAA) [2, 3, 4, 5, 6, 7]. This approach is preferred because directly resolving sound propagation within the flow field requires extremely high mesh resolution extending to the far-field region of interest. Such requirements substantially increase computational costs. According to CFD Vision 2030 [8], hybrid RANS/LES and wall-modeled LES (WMLES) are the most promising techniques for predicting aviation outflow fields under high Reynolds numbers (Re). These methods effectively model the boundary layer and reduce mesh requirements in the vicinity of the wall. In contrast, the report and several recent studies [9, 10, 11, 12, 13, 14] indicate that wall-resolved LES (WRLES) will remain impractical for engineering applications in the foreseeable future. Zhang et al. [9] believe that it may take several decades before the complete numerical method can accurately predict the noise generated by high-lift devices, primarily due to computational cost constraints.

Recent developments in high-order methods, particularly discontinuous Galerkin (DG) [15, 16, 17], flux reconstruction (FR) [18, 19, 20], and correction procedure via reconstruction (CPR) [21, 22] methods, enable dramatic reductions in mesh quantity and computational expenditure. Such improvements progressively enhance the practicality of LES simulations. Particularly, DIMAXER, our self-developed commercial solver, employs the space-time expansion of the high-order kinetic-preserving FR (STE-KEP-FR) scheme [2, 19, 20]. This scheme combines the advantages of the simple differential form of the high-order FR scheme [18], a one-step time integration approach that enables time-accurate local time stepping [23, 24], and enhanced nonlinear stability achieved by adopting a split-form kinetic-preserving method to treat the convective term [25]. The STE-KEP-FR scheme significantly reduces the number of required mesh elements while improving simulation accuracy on flow fields. More importantly, it allows for local time stepping for each mesh element, in contrast to traditional methods that force faster computing elements to wait for the slowest ones. Modern GPU acceleration further reduces computational expenses and simulation times compared to CPU-based solvers.

Recently, Zhang et al. [2] utilized DIMAXER to conduct WRLES on the 30P30N high-lift airfoil benchmark with only 74 GPU hours for 10 flow pass times (FPTs, based on stowed chord length c_s) under a Reynolds number of 1.71×10^6. Excellent agreements with multiple experimental and numerical datasets are achieved. In contrast, Asada et al. [26] carried out WMLES on the same benchmark case with a second-order scheme, which costs 1,152 CPU nodes (55,296 CPU cores). This is remarkable given the prediction by Spalart and Philippe [27] in 2000 that quasi-direct numerical simulation (QDNS), or WRLES [28], would not be feasible for industrial applications until 2070. In addition, they [28] later believed that this estimate was overly optimistic due to the decline of Moore's Law. However, DIMAXER has the potential to accelerate this timeline in the coming years.

In the present study, the 30P30N high-lift airfoil and Trap Wing semi-span model are utilized to evaluate the noise prediction ability of DIMAXER on high-lift devices. A direct comparison is conducted between DIMAXER and the second-order CPU-based finite volume (FV) solver OpenCFD-EC [29] for the 30P30N benchmark case. The Trap Wing model is used to illustrate that performing WRLES on a 3D aircraft is no longer impractical. Both cases feature a Reynolds number in the millions, and the simulations are conducted on a GPU node equipped with RTX 4090D GPUs.

This paper is organized as follows: Sec. 2 offers a brief overview of the numerical scheme and the method for predicting far-field noise. Sec. 3 discusses the flow field and aeroacoustic results for the two benchmark cases accordingly. Lastly, Sec. 4 summarizes the main conclusions and future perspectives.

2. Numerical methods

2.1 Governing equations for weakly compressible flow

The spatially filtered continuity and momentum equations of the Navier-Stokes equations can be written as:

$$\frac{\partial \rho}{\partial t} + \frac{\partial (\rho u_i)}{\partial x_i} = 0 \tag{1}$$

$$\frac{\partial (\rho u_i)}{\partial t} + \frac{\partial (\rho u_i u_j)}{\partial x_j} + \frac{\partial p}{\partial x_i} = \frac{\partial \tau_{ij}}{\partial x_j} \tag{2}$$

where ρ denotes the density, u_i denotes the velocity component, p denotes the pressure, and τ_{ij} is the viscous stress tensor, which has the form of:

$$\tau_{ij} = (\mu + \mu_{sgs})(S_{ij} - \frac{1}{3} S_{kk} \delta_{ij}) \tag{3}$$

$$S_{ij} = \frac{1}{2}\left(\frac{\partial u_i}{\partial x_j} + \frac{\partial u_j}{\partial x_i}\right) \tag{4}$$

with μ denotes the physical viscosity and remains constant for weakly compressible flow, μ_{sgs} denotes the subgrid-scale viscosity, δ_{ij} is the Kronecker delta.

Considering weakly compressible flow, p is only a function of ρ, the barotropic gas state equation [30] can be used:

$$p(\rho) = c_0^2 (\rho - \rho_0) + p_0 \tag{5}$$

with c_0, ρ_0 and p_0 denoting the far-field speed of sound, density, and pressure, respectively.

2.2 Governing equations for compressible flow

The full Navier-Stokes equations are Eqs. 1 and 2 plus energy equation:

$$\frac{\partial E}{\partial t} + \frac{\partial (E+p)u_j}{\partial x_j} = \frac{\partial u_i \tau_{ij}}{\partial x_j} - \frac{\partial q_j}{\partial x_j} \tag{6}$$

where E is the total energy and q_j is the heat flux, which has the form of:

$$q_j = -(\kappa + \kappa_{sgs}) \frac{\partial T}{\partial x_j} \tag{7}$$

with T denotes the temperature, κ denotes the thermal conductivity coefficient and equals to $\mu c_p / Pr$, κ_{sgs} denotes the subgrid-scale thermal conductivity coefficient and equals to $\mu_{sgs} c_p / Pr_t$, and c_p is the heat capacity at constant pressure. The Prandtl number Pr and the turbulent Prandtl number Pr_t are equals to 0.72 and 0.9, respectively.

For compressible flow, the physical viscosity is computed using the Sutherland's law:

$$\mu = \mu_0 \left(\frac{T}{T_0} \right)^{\frac{3}{2}} \frac{T_0 + S}{T + S} \tag{8}$$

with $\mu_0 = 1.716 \times 10^{-5} Pa \cdot s$, $T_0 = 273.15K$, and $S = 110.55K$.

In addition, ideal gas law is employed to compute the total energy:

$$p = \rho R T \tag{9}$$

$$E = \frac{p}{\gamma - 1} + \frac{1}{2} \rho u_i u_i \tag{10}$$

where R is the gas constant, and γ is set to 1.4 for compressible flow.

2.3 Subgrid-scale model

To close the above governing equations, wall-adaptive local eddy-viscosity (WALE) model [31] is employed:

$$\mu_{sgs} = \rho (C_w \Delta)^2 \frac{(S_{ij}^d S_{ij}^d)^{3/2}}{(S_{ij} S_{ij})^{5/2} + (S_{ij}^d S_{ij}^d)^{5/4}} \tag{11}$$

where C_w denotes the model coefficient, taking values 0.12 and 0.2 for the 30P30N and Trap Wing benchmarks, respectively. $\Delta = (\text{cell volume})^{1/3}$ is the mesh element size, and S_{ij}^d is the traceless symmetric part of the square of the velocity gradient tensor:

$$S_{ij}^d = \frac{1}{2} \left(\frac{\partial u_i}{\partial x_k} \frac{\partial u_k}{\partial x_j} + \frac{\partial u_j}{\partial x_k} \frac{\partial u_k}{\partial x_i} \right) - \frac{1}{3} \delta_{ij} \frac{\partial u_l}{\partial x_k} \frac{\partial u_k}{\partial x_l} \tag{12}$$

2.4 STE-KEP-FR Scheme

To briefly review the STE-KEP-FR scheme, first rewrite the governing equations to conservative form:

$$\frac{\partial \boldsymbol{U}}{\partial t} + \nabla^{\boldsymbol{x}} \cdot \boldsymbol{F}^{\boldsymbol{x}} = 0 \tag{13}$$

where $\boldsymbol{U}$ denotes conservation variable matrix in Cartesian domain, $\boldsymbol{x}$ denotes Cartesian domain coordinate vector, and $\boldsymbol{F}$ represents flux matrix. For weakly compressible flow:

$$\boldsymbol{U} = \begin{bmatrix} \rho \\ \rho u \\ \rho v \\ \rho w \end{bmatrix}, \quad \boldsymbol{F}^{\boldsymbol{x}} = \begin{bmatrix} \rho u_i \\ \rho u_i u + p\delta_{i1} - \tau_{i1} \\ \rho u_i v + p\delta_{i2} - \tau_{i2} \\ \rho u_i w + p\delta_{i3} - \tau_{i3} \end{bmatrix} \tag{14}$$

for compressible flow:

$$\boldsymbol{U} = \begin{bmatrix} \rho \\ \rho u \\ \rho v \\ \rho w \\ E \end{bmatrix}, \quad \boldsymbol{F}^{\boldsymbol{x}} = \begin{bmatrix} \rho u_i \\ \rho u_i u + p\delta_{i1} - \tau_{i1} \\ \rho u_i v + p\delta_{i2} - \tau_{i2} \\ \rho u_i w + p\delta_{i3} - \tau_{i3} \\ \rho u_i (E + p) - u_j \tau_{ij} + q_i \end{bmatrix} \tag{15}$$

The coordinate transformation from Cartesian to computational domain can be described as:

$$\widehat{\boldsymbol{U}} = |J|\boldsymbol{U} \tag{16}$$

$$\boldsymbol{F}^{\xi} = |\boldsymbol{J}|\left(\xi_x \boldsymbol{F}^x + \xi_y \boldsymbol{F}^y + \xi_z \boldsymbol{F}^z\right) \tag{17}$$

$$\boldsymbol{F}^{\eta} = |\boldsymbol{J}|\left(\eta_x \boldsymbol{F}^x + \eta_y \boldsymbol{F}^y + \eta_z \boldsymbol{F}^z\right) \tag{18}$$

$$\boldsymbol{F}^{\zeta} = |\boldsymbol{J}|\left(\zeta_x \boldsymbol{F}^x + \zeta_y \boldsymbol{F}^y + \zeta_z \boldsymbol{F}^z\right) \tag{19}$$

where (x, y, z) is the Cartesian domain coordinate, (ξ, η, ζ) is the computational domain coordinate, and $\boldsymbol{J}$ is the Jacobian matrix given by:

$$J = \begin{vmatrix} x_\xi & x_\eta & x_\zeta \\ y_\xi & y_\eta & y_\zeta \\ z_\xi & z_\eta & z_\zeta \end{vmatrix} \tag{20}$$

Then Eq. (13) in computational domain can be written as:

$$\frac{\partial \widehat{\boldsymbol{U}}}{\partial t} + \nabla^{\xi} \cdot \boldsymbol{F}^{\xi} = 0 \tag{21}$$

A schematic of using Lagrange-Gauss-Legendre (LGL) points as the solution points for a hexahedral element is shown in Fig. 1. For the k^{th} solution point of the j^{th} element, the uniform FR scheme is given as:

$$\frac{\partial \hat{\boldsymbol{U}}_{j,k}}{\partial t} + \left(\nabla^{\xi} \cdot \boldsymbol{F}^{\xi}(\boldsymbol{U}_j)\right)_{j,k} + \sum_{s=1}^{N_s} \sum_{f=1}^{N_f} \alpha_{k,s,f} \left(\widetilde{\boldsymbol{F}}^{\xi}|_n - \boldsymbol{F}^{\xi}|_n\right)_{k,s,f} = 0 \tag{22}$$

where N_s is the number of element interfaces, N_f is the number of flux points on the interface. For the common flux matrix $\widetilde{\boldsymbol{F}}$, the nonlinear inviscid flux is computed by the HLLC Riemann solver [32], while the viscous flux is treated with the interior penalty method [33]. $\boldsymbol{F}|_n = \boldsymbol{F} \cdot \boldsymbol{n}$ where n is outer normal unit vector at each flux point. The difference between the common flux and the outer normal projection of local flux is referred to as correction flux. The g2 correction function [18] is employed with the FR coefficient α being specified. The convective term (excluding pressure) of the divergence component in the governing equations is computed using the KEP split-form scheme developed by Feiereisen [34].

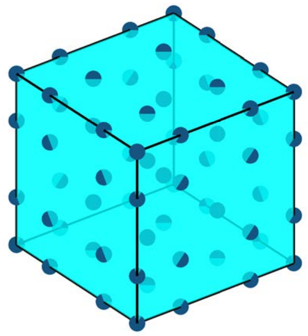

(a)

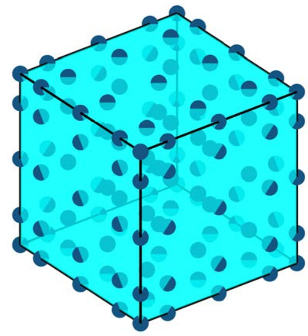

(b)

Figure 1: Distribution of LGL solution points for a hexahedral element with (a) 3^{rd} degree polynomial reconstruction (K = 3, 4^{th} order of accuracy), (b) 4^{th} degree polynomial reconstruction (K = 4, 5^{th} order of accuracy).

A local time stepping strategy is implemented following the approach proposed by Gassner et al. [23, 24] for discontinuous Galerkin methods. Eq. (22) is rewritten in the following form:

$$\frac{\partial \boldsymbol{U}_{j,k}}{\partial t} = \mathbb{R}^{Div}_{j,k}(\boldsymbol{U}_j) + \sum_{s=1}^{N_s}\sum_{f=1}^{N_f} \mathbb{R}^{Cor}_{j,k,s,f}(\boldsymbol{U}_j) \tag{23}$$

$$\mathbb{R}^{Div}_{j,k}(\boldsymbol{U}_j) = -\frac{1}{|\boldsymbol{J}|_{j,k}} \left(\nabla^{\xi} \cdot \boldsymbol{F}^{\xi}(\boldsymbol{U}_i)\right)_{j,k} \tag{24}$$

$$\mathbb{R}^{Cor}_{j,k,s,f}(\boldsymbol{U}_j) = -\frac{1}{|\boldsymbol{J}|_{j,k}} \alpha_{k,s,f} \left(\widetilde{\boldsymbol{F}}^{\xi}|_n(\boldsymbol{U}_j) - \boldsymbol{F}^{\xi}|_n(\boldsymbol{U}_j)\right)_{k,s,f} \tag{25}$$

where $\mathbb{R}^{Div}$ represents the flux divergence term, while $\mathbb{R}^{Cor}$ represents a linear combination of the correction flux terms.

The integration of equation Eq. (23) over $[t^n, t^{n+1}]$ results in:

$$\boldsymbol{U}^{n+1}_{j,k} - \boldsymbol{U}^{n}_{j,k} = \int_{t^n}^{t^{n+1}} \left[\mathbb{R}^{Div}_{j,k}(\boldsymbol{U}_j) + \sum_{s=1}^{N_s}\sum_{f=1}^{N_f} \mathbb{R}^{Cor}_{j,k,s,f}(\boldsymbol{U}_j)\right] dt \tag{26}$$

Within the temporal interval $t \in [t^n, t^{n+1}]$, the local space-time prediction $\boldsymbol{v}_j = \boldsymbol{v}(\boldsymbol{x}_j, t)$ is established. The 6-stage and 8-stage continuous explicit Runge-Kutta (CERK) schemes [35] discretize K3 and K4 simulations, respectively, with a CFL number of $\frac{0.8}{2K+1}$. A time-dependent equation is solved:

$$\frac{d\boldsymbol{v}_{j,k}}{dt} = \mathbb{R}^{Div}_{j,k}\left(\boldsymbol{v}(\boldsymbol{x}_j, t)\right) \tag{27}$$

with an initial condition given by $\boldsymbol{v}(\boldsymbol{x}_j, t = t^n) = \boldsymbol{U}^n_j$.

The temporal integration of Eq. (26) follows a two-stage predictor-corrector framework. The prediction stage computes the next time step results through the CERK scheme in Eq. (27) using intra-element information. Correction then proceeds via 5^{th} Gaussian quadrature based on the predicted solution. This procedure yields the final equation:

$$\boldsymbol{U}^{n+1}_{j,k} = \boldsymbol{v}_{j,k}(t^{n+1}) + \sum_{s=1}^{N_s}\sum_{f=1}^{N_f}\sum_{qp}^{N^t_{qp}} \Delta t \cdot w^t_{qp} \mathbb{R}^{Cor}_{j,k,s,f}\left(\boldsymbol{v}_j(t_{qp})\right) \tag{28}$$

where N^t_{qp} denotes the number of time quadrature point while Δt denotes the time step. The nondimensional weight w^t_{qp} is obtained from Gaussian quadrature coefficients, $\tau_{qp} \in [0, 1]$ is the corresponding Gaussian node, and the physical time is given by $t_{qp} = t^n + \Delta t \cdot \tau_{qp}$.

2.5 FW-H acoustic analogy

A customized OpenCFD-FWH [2, 36] version is employed for far-field noise predictions. This version incorporates parallel I/O capabilities to accelerate the computational process. The implementation accounts for incoming flow effects and takes the following form:

$$\begin{aligned} 4\pi p'(\boldsymbol{x},t) = &\int_{f=0}\left[\frac{\dot{Q}_i n_i}{R(1-M_R)^2}\right]_{ret} dS + \int_{f=0}\left[\frac{Q_n c_0(M_R - M^2)}{R^2(1-M_R)^3}\right]_{ret} dS \\ &+ \frac{1}{c_0}\int_{f=0}\left[\frac{\dot{L}_R}{R(1-M_R)^2}\right]_{ret} dS + \int_{f=0}\left[\frac{L_R - L_M}{R^2(1-M_R)^2}\right]_{ret} dS \\ &+ \int_{f=0}\left[\frac{L_R(M_R - M^2)}{R^2(1-M_R)^3}\right]_{ret} dS \end{aligned} \tag{29}$$

where p' is the sound pressure, $\boldsymbol{x}$ is the coordinate vector of the observer, M is the Mach number (Ma) of the moving surface relative to the inflow, M_i represents the component of M, and $f = 0$ represents the moving surface such that the unit outward normal of the surface $\boldsymbol{n} = \nabla f$. The overdot "$\cdot$" indicates differentiation with respect to the source time τ, and terms enclosed in brackets with the subscript ret are evaluated at the retarded time $\tau_{ret} = t - R/c_0$.

Consider an inflow having an angle-of-attack (AoA) within the x-y plane. The associated quantities Q_n, L_R, M_R, and the effective acoustic distance R are given by:

$$Q_n = Q_i n_i = [-\rho_0 U_{0i} + \rho u_i]\, n_i \tag{30}$$

$$L_R = L_i \hat{R}_i = [(p - p_0)\delta_{ij} + \rho(u_i - U_{0i})u_j] n_j \hat{R}_i \tag{31}$$

$$M_R = M_i \hat{R}_i \tag{32}$$

where U_{0i} is the velocity component of the inflow, and other corresponding variables are defined as:

$$\hat{R}_1 = \frac{-M_0 R^* + d_1}{(1-M_0)R}\cos(\mathrm{AoA}) - \frac{d_2}{R}\sin(\mathrm{AoA}) \tag{33}$$

$$\hat{R}_2 = \frac{-M_0 R^* + d_1}{(1-M_0)R}\sin(\mathrm{AoA}) + \frac{d_2}{R}\cos(\mathrm{AoA}) \tag{34}$$

$$\hat{R}_3 = d_3/R \tag{35}$$

$$R = \frac{-M_0 cos(\mathrm{AoA}) d_1 - M_0 sin(\mathrm{AoA}) d_2 + R^*}{1 - M_0^2} \tag{36}$$

$$R^* = \sqrt{(M_0 cos(\mathrm{AoA}) d_1 + M_0 sin(\mathrm{AoA}) d_2)^2 + \beta^2 [d_1^2 + d_2^2 + d_3^2]} \tag{37}$$

$$d_1 = (x_1 - y_1)\cos(\mathrm{AoA}) + (x_2 - y_2)\sin(\mathrm{AoA}) \tag{38}$$

$$d_2 = -(x_1 - y_1)\sin(\mathrm{AoA}) + (x_2 - y_2)\cos(\mathrm{AoA}) \tag{39}$$

$$d_3 = (x_3 - y_3) \tag{40}$$

The solid FW-H sampling surface is employed in the present study by setting the surface velocity to zero in Eq. (29).

3. Results and discussions

3.1 30P30N high-lift airfoil benchmark

30P30N high-lift airfoil slat noise is an important CAA benchmark problem from the 3^{rd} AIAA Workshop on Benchmark Problems for Airframe Noise Computations (BANC-III) [37]. This classic high-lift airfoil was developed by McDonnell Douglas in the early 1990s and has been widely studied in academic research, especially with regard to slat noise [2, 4, 6, 7, 26, 37, 38, 39, 40, 41, 42, 43, 44, 45, 46].

A modified version of the 30P30N airfoil created by Japan Aerospace Exploration Agency (JAXA) [38, 39] is used and its profile can be seen in Fig. 2a. Its c_s is 0.4572 m, and the slat and flap both deflect 30° with corresponding chord lengths of $0.15c_s$ and $0.3c_s$, respectively. The Reynolds number based on c_s is equal to 1.71×10^6 under Ma = 0.17 and the freestream incidence angle is specified as 5.5°.

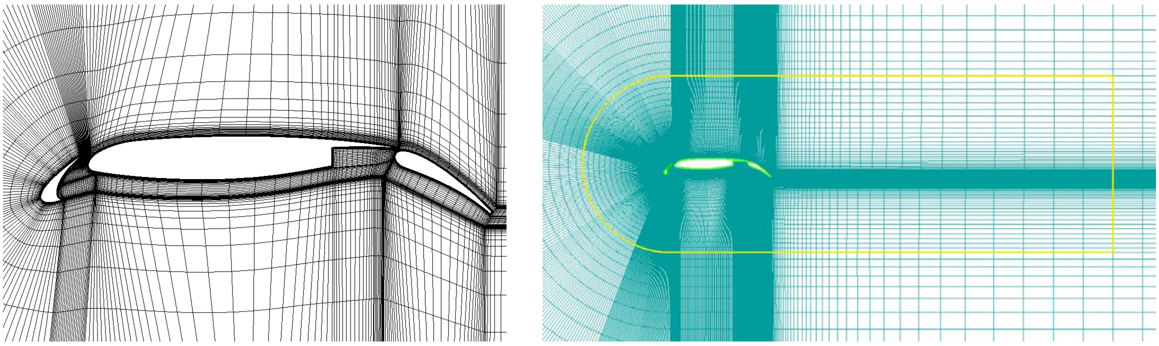

(a) (b)

Figure 2: Mesh details of the 30P30N benchmark case. (a) DIMAXER configuration; (b) OpenCFD-EC configuration.

The coarse mesh from Zhang et al. [2] has been used for the DIMAXER K4 weakly compressible solver. Comparative simulations are conducted using OpenCFD-EC [29, 36] with improved delayed detached-eddy simulation (IDDES). This solver represents a conventional K1 (2^{nd} order) finite volume method implemented on CPU nodes. Both meshes employ C-type topology and feature a spanwise length of $1/9c_s$, following the BANC-III recommendation [37]. An overview of the mesh configurations is shown in Fig. 2. Detailed mesh setting comparisons are listed in Table 1.

Table 1: Mesh setting of the 30P30N benchmark case.

Solver	Order	Mesh quantity	DoFs	y^+_{mesh}	$y^+ = \frac{y^+_{mesh}}{K+1}$ [11]
DIMAXER	K4	250,784	31.3 million	< 10	< 2
OpenCFD-EC	K1	43.6 million	43.6 million	< 2	< 1

For turbulent flow simulations, traditional K1 methods usually characterize mesh resolution requirements through nondimensional mesh spacing metrics: x^+_{mesh} (streamwise), y^+_{mesh} (wall-normal), and z^+_{mesh} (spanwise). However, for high-order methods with substantially more DoFs per element, the mesh resolution requires scaling by a factor of $K + 1$ to better represent the actual resolution [22]. Wang and Hantla [22] further showed that simulations using K3 and K5 schemes with $y^+ = \frac{y^+_{mesh}}{3+1} = 40$ and $y^+ = \frac{y^+_{mesh}}{5+1} = 54$, respectively, yield results equivalent to those obtained from K1 simulations with $y^+ \leq 10$.

The wall-unit distributions from the K4 WRLES simulation are displayed in Fig. 3. Even when scaled according to the K3 standard of $1/4$, these results fully satisfy the WRLES criteria established by [47], i.e. $50 \leq x^+ \leq 150$, $y^+ \leq 1$, $15 \leq z^+ \leq 40$.

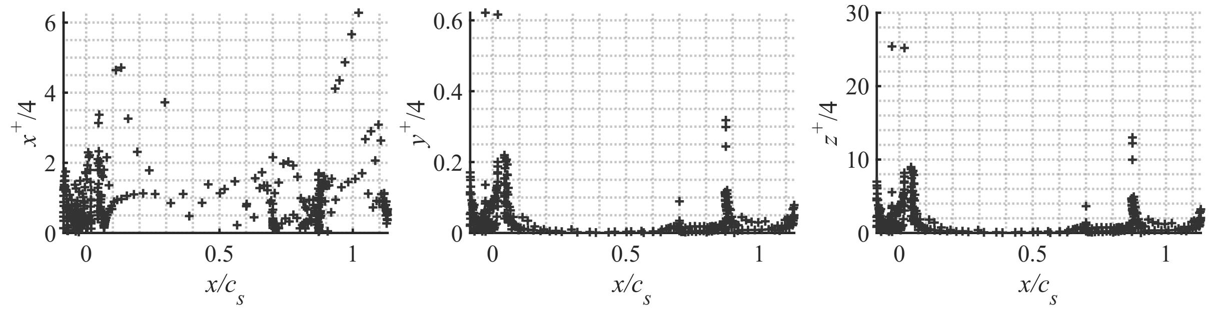

Figure 3: Wall-unit distributions from the K4 WRLES simulation of the 30P30N benchmark case.

Table 2: Computational cost and lift performance of 30P30N benchmark cases compared with JAXA RANS simulation [39].

Solver	Method	Hardware	Cost for 1FPT	$C_L(Ratio_{\Delta C_L})$
DIMAXER	K4 WRLES	RTX 4090D*4	16 GPU hours	2.87(-1.3%)
OpenCFD-EC	IDDES	3000 CPU cores	47k CPU core hours	2.62(-10.0%)

The computational domain for WRLES extends $50c_s$ in the forward as well as the vertical directions, and $60c_s$ in the rear direction. While the computational domain for IDDES extends $45c_s$ in the forward as well as the vertical directions, and $67.5c_s$ in the rear direction. In the WRLES setup, non-reflective boundary conditions are applied along the x and y directions. For the IDDES setup, a sponge layer is adopted to suppress boundary-induced reflections. The detailed implementation procedures are described in [2] and [36], respectively. Both cases have periodic boundary conditions applied on the spanwise direction (z direction).

The flow field of each simulation is initialized by a RANS solution to speed up the convergence process. As previously mentioned, CERK is utilized to explicitly advance the time step on local elements. For IDDES, implicit dual-time LU-SGS method is implemented for time advancement, employing a time step of $2 \times 10^{-7}s$ with five inner sub-iterations. Both cases are computed until the flow field is stable, with an additional 6 FPTs used for data processing. Furthermore, the acoustic data is sampled at a rate of 100 kHz for both cases. Acoustic signals are analyzed via periodogram method with a Hanning window and 50% overlap, yielding a frequency resolution of 100 Hz. Additionally, the computational mesh is refined into sub-elements of order K^3 to enable high-order flow field visualization, following the implementation of [2, 22].

Computational resources and lift coefficient (C_L) data are summarized in Table 2. The IDDES case employed SunRising platform CPU nodes. Each node comprised a 32-core x86 processor at 2.0 GHz base frequency. The simulation used 120 nodes with 25 cores per node. K4 WRLES achieved 1 FPT using 4 RTX 4090D GPUs over 4 hours, whereas IDDES consumed 47k CPU core-hours. K4 WRLES demonstrates higher accuracy than IDDES based on C_L comparisons. IDDES exhibits systematic underestimation of negative pressure on airfoil upper surfaces, as demonstrated in Fig. 4. Furthermore, IDDES predictions of pressure coefficient (C_p) distributions align more closely with JAXA experimental measurement [39] within the slat cove area. Meanwhile the K4 WRLES simulation exhibits better consistency with FSU experimental data [41].

Fig. 5 compares the wall pressure fluctuation spectra with experimental data from [38, 39, 40, 41] and numerical predictions from [4, 6, 7, 26]. At probe S3, where impingement occurs under 5.5° AoA, a broadband spectrum is observed. Excellent agreement with experimental and numerical data is achieved by the K4 WRLES, while the IDDES spectrum decays rapidly beyond 2 kHz. This trend continues at probes S10 and M7, where K4 WRLES consistently matches the datasets. The IDDES method, however, provides inferior predictions for tonal noise and exhibits a rapid high-frequency decay.

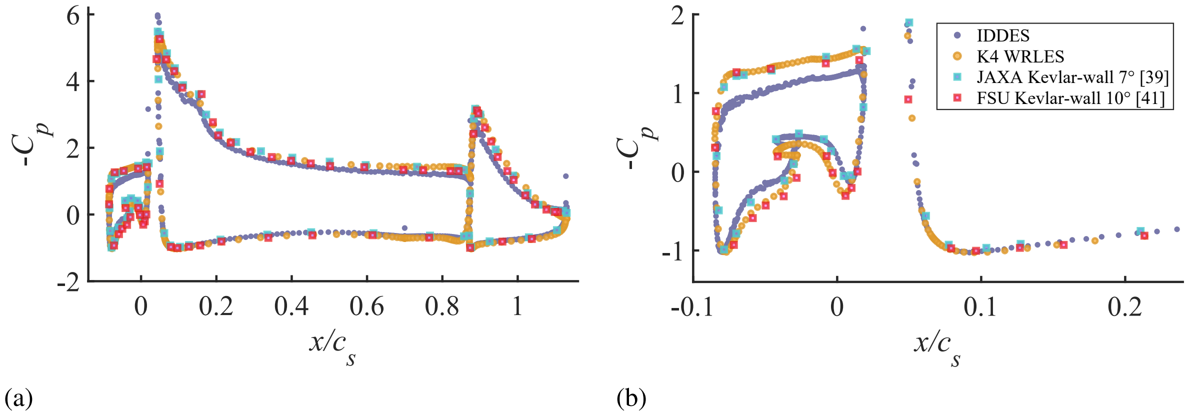

Figure 4: Comparison of time-averaged C_p distributions with Kevlar-wall experiments from JAXA [39] and FSU [41]. (a) C_p distributions on all three elements; (b) around slat.

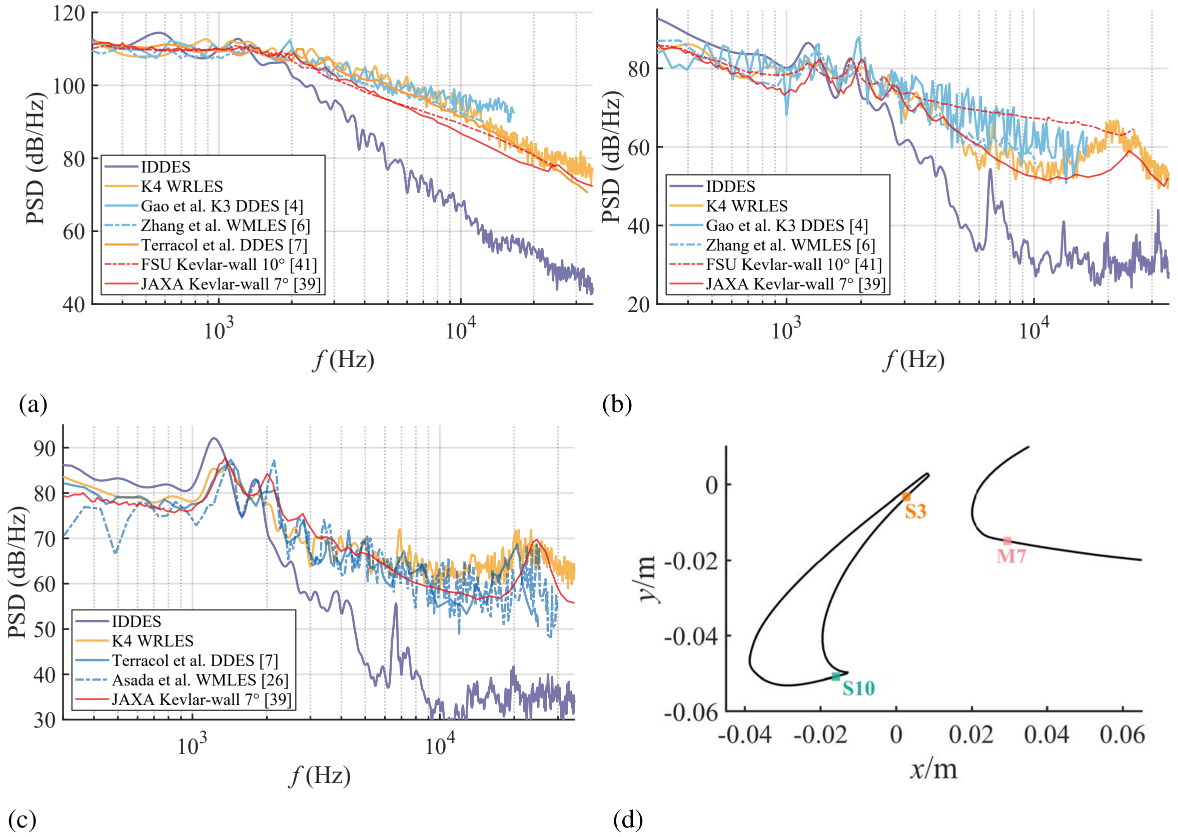

Figure 5: Wall pressure spectra compared with experimental and numerical results at (a) probe S3; (b) probe S10; (c) probe M7. (d) Probe locations on the airfoil midplane.

Far-field noise predictions in the K4 WRLES simulation use the slat surface for FW-H sampling, consistent with best practices for high-order WRLES simulations [2]. For the IDDES simulation, a porous surface is adopted, as shown by the yellow line in Fig. 2b, with endcap omitted. Far-field noise spectra are shown in Fig. 6. DIMAXER provides accurate predictions of the far-field noise spectrum. The OpenCFD-EC with IDDES is relatively ineffective in capturing the first two tonal noise frequencies, as also observed in the wall pressure spectra. Nonetheless, relatively good agreements are obtained below 10 kHz for the broadband amplitude, suggesting that high-frequency broadband pressure fluctuations observed in the wall pressure spectra have minimal impact on far-field slat noise. Hybrid RANS/LES methods remain suitable for this type of aeroacoustic prediction despite losing turbulence information through RANS modeling of the boundary layer. Similar conclusions were drawn by Manoha and Caruelle [48].

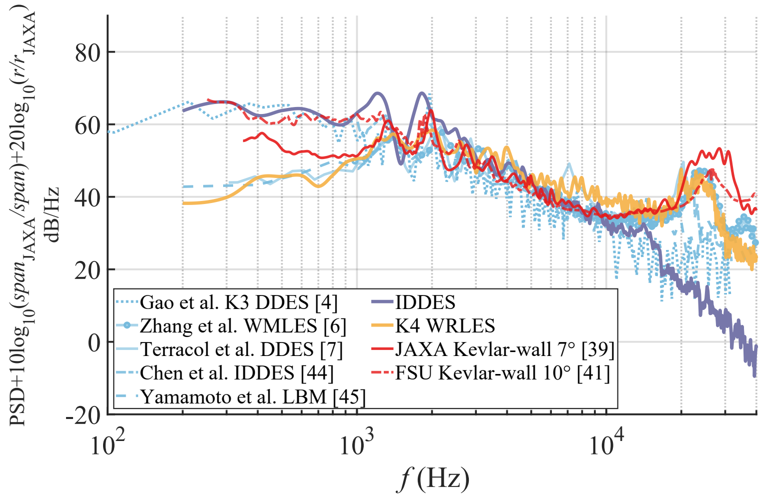

Figure 6: Far-field noise spectrum at the phased microphone array center of JAXA experiments [38, 39] in comparison with numerical [4, 6, 7, 44, 45] and experimental [39, 41] datasets.

Fig. 7 shows instantaneous contours of nondimensional spanwise vorticity ($C_{\omega z} = \omega_z c_s / U_0$, ω_z is the spanwise vorticity) within the slat cove region. The K4 WRLES simulation achieves much finer flow field resolution than the conventional second-order FV method with IDDES simulation.

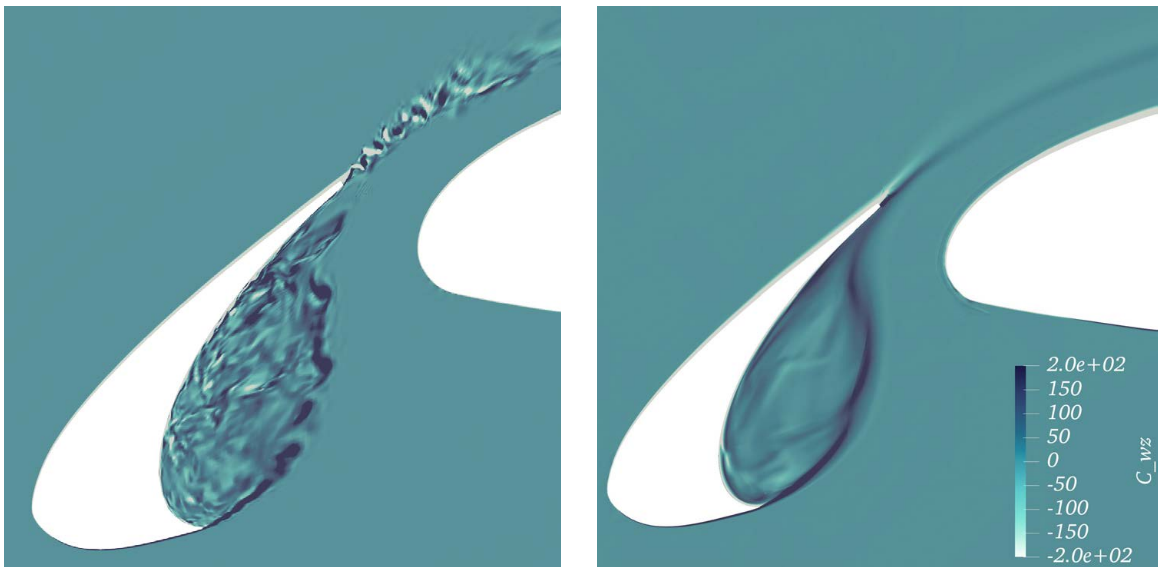

(a) (b)

Figure 7: Contours of instantaneous normalized spanwise vorticity $C_{\omega z}$ on the 30P30N airfoil midplane plane from (a) K4 WRLES; (b) IDDES.

Overall, DIMAXER achieves 1FPT K4 WRLES flow field for the 30P30N high-lift airfoil using only four RTX 4090D GPU cards within 4 hours. In contrast, a traditional second-order FV solver performing IDDES requires hundreds of CPU nodes and thousands of CPU cores with four times the hardware wall time. Even more demanding, Asada et al. [26] utilized thousands of CPU nodes and tens of thousands of CPU cores for WMLES with a second-order FV solver. Crucially, DIMAXER exhibits better agreement with experimental data and substantially enhanced flow field resolution, demonstrating its superiority for high-lift airfoil aeroacoustic investigations.

3.2 Trap Wing semi-span model

The Trap Wing semi-span models are a series of simplified three-element high-lift configurations with a slat, a swept main wing, and a flap mounted to a flat-sided body, developed by NASA. The one equipped with the full flap is studied in the 1^{st} AIAA CFD High Lift Prediction Workshop (HLPW-1) [49].

“Config 1” from HLPW-1 is selected to perform WRLES. It has a mean aerodynamic chord (MAC) of 1.006 m, with the deflection angles of the slat and flap are $\delta_s = 30°$ and $\delta_f = 25°$, respectively, as shown in Fig. 8. At a Mach number of 0.2, the corresponding Reynolds number based on the MAC is 4.30×10^6. Additional geometric information can be found in the article from Streett et al. [50].

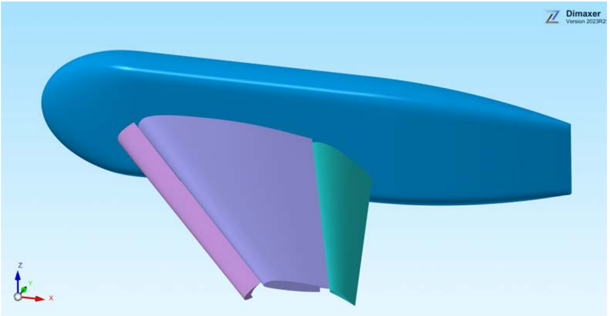

Figure 8: “Config 1” model from HLPW-1.

A structural mesh comprising 5.1 million elements is generated as illustrated in Fig. 9. The computational domain is defined as a hemisphere with a radius of 72 MAC. Non-reflective boundary condition is implemented at the far-field boundary, while symmetry condition is imposed on the symmetry plane.

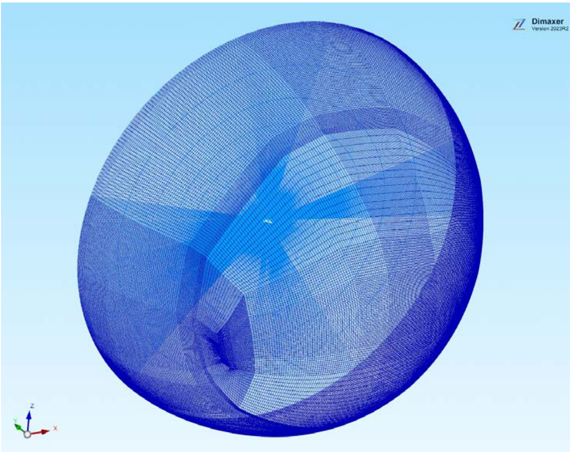

(a)

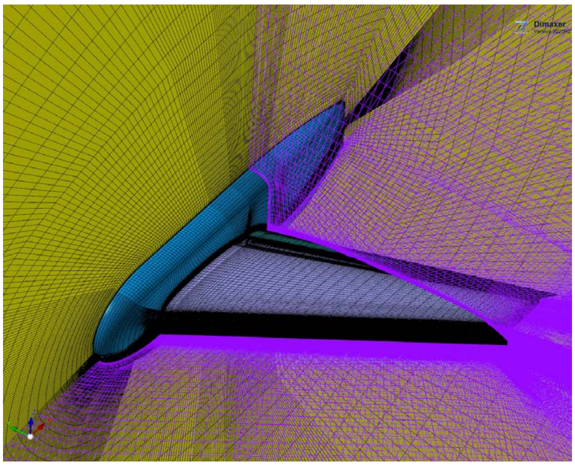

(b)

Figure 9: Mesh setup for the Trap Wing model. (a) Computation domain; (b) near wall mesh.

The inflow incidence is 13°, which is a typical task for "Config 1" in HLPW-1. Similarly, a RANS solution is employed as the initial condition, and the simulation is performed using the DIMAXER compressible K3 solver with 0.32 billion DoFs. Flow field analysis utilizes data from the final 6 FPTs (based on MAC), with a sampling rate of 100 kHz. A computational node comprising 8 RTX 4090D GPUs requires 35.7 hours to produce 1 FPT of flow field data.

The maximum equivalent K1 values satisfy $y^+ < 1$ and $x^+/z^+ < 110$ (computed through the square root of the sub-face area). Resolution requirements for y^+ and x^+ follow WRLES criteria [47], while the z^+ resolution exceeds requirements by a factor of three. This mesh represents the finest mesh resolution achievable within current computational resources and practical wall time constraints.

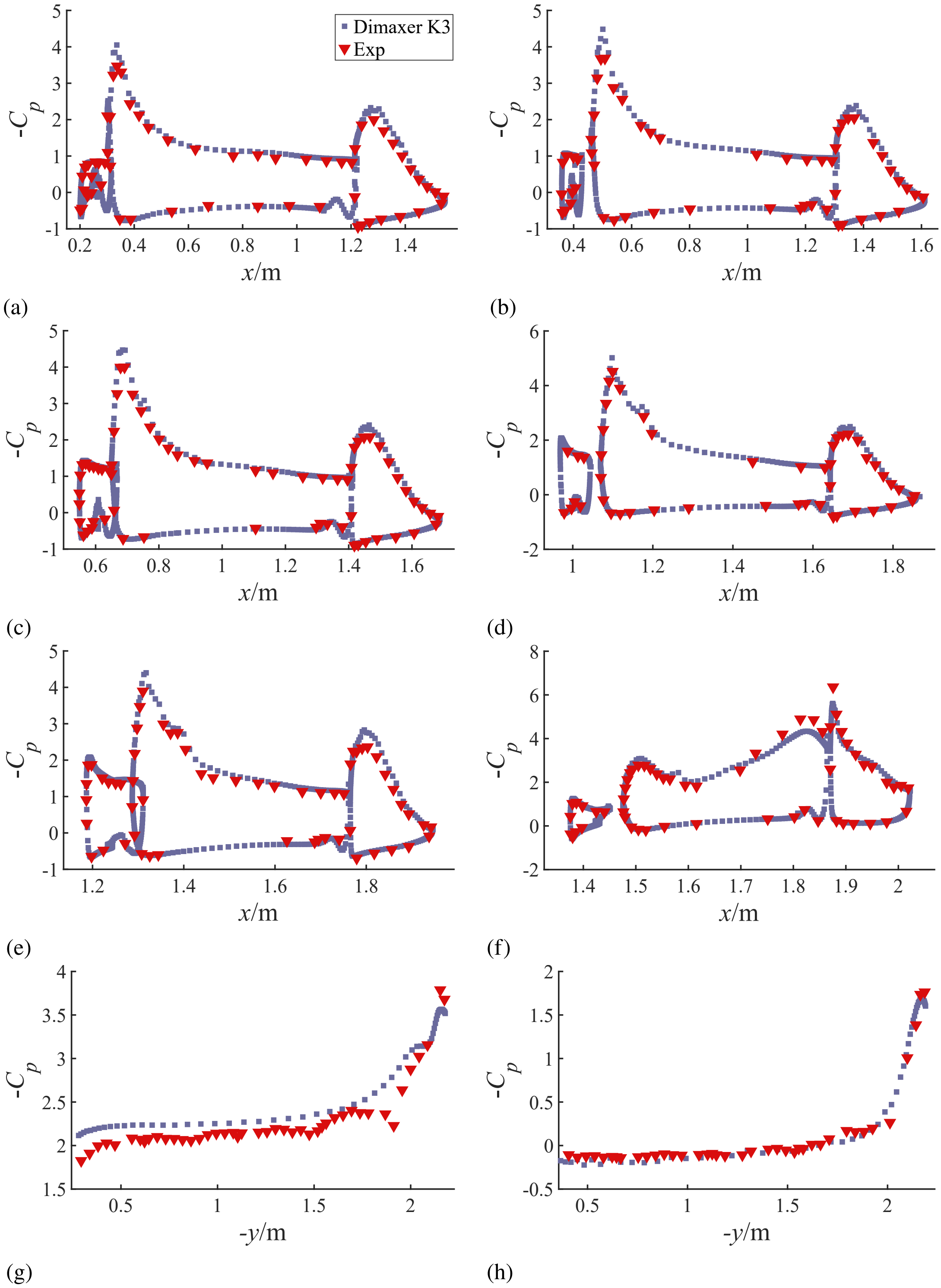

Figure 10: Time-averaged C_p distribution compared with HLPW-1 experiment results [49] at (a) η = 17%; (b) η = 28%; (c) η = 41%; (d) η = 70%; (e) η = 85%; (f) η = 98%; (g) flap fwd span; (h) flap aft span.

Table 3 presents the aerodynamic force results alongside experimental data provided by HLPW-1 [49]. DIMAXER predicts a higher lift coefficient (C_L) with a difference of 4.75%. Regarding the C_p distribution in Fig. 10, a slightly higher prediction of the flap negative pressure across the entire wing can be observed. As noted in the post-workshop summary [49], the C_L result from CFD for the no-bracket clean wing is expected to be higher than the experimental data, which includes the effects of brackets. Consequently, the higher C_L and C_p prediction from DIMAXER is justifiable. The influence of the brackets is evident in Fig. 10g. Additionally, the results from the K3 simulation align closely with the experimental C_p distribution up to the tip of the flap aft span, which is much better than a RANS outcome from the workshop with a mesh exceeding 0.28 billion elements [51]. Besides, Fig. 10f reveals an underprediction of negative pressure near the wing tip. Similar trends are observed in results from all other workshop participants. For the drag coefficient (C_D), result from DIMAXER agrees well with experimental data, exhibiting a 2.62% error. DIMAXER predictions for the moment coefficient (C_M) deviate by 6.02% from experimental measurements. This deviation arises due to bracket omission in the simulation model. Consequently, the upper flap surface experiences higher negative pressure as mentioned before, resulting in a more pronounced nose-down pitching moment.

Table 3: Aerodynamic results of Trap Wing from K3 simulation compared with experimental data [49].

	$C_L(Ratio_{\Delta_{C_L}})$	$C_D(Ratio_{\Delta_{C_D}})$	$C_M(Ratio_{\Delta_{C_M}})$
Exp	2.047	0.333	-0.503
K3 simulation	2.145(4.76%)	0.342(2.52%)	-0.533(6.06%)
Exp lower	2.014(-1.63%)	0.327(-1.86%)	-0.487(2.15%)
Exp upper	2.070(1.10%)	0.343(2.94%)	-0.514(-3.22%)

The K3 simulation accurately captures the transition location on the upper surface of each wing element, consistent with results from Eliasson et al. [52], as demonstrated in Fig. 11. Accurate prediction of transition locations represents a critical aspect of high-lift device simulations [53].

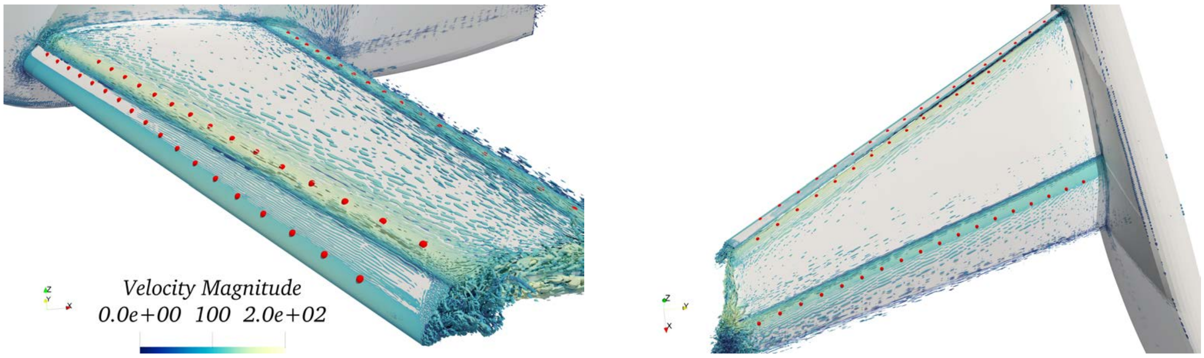

(a) (b)

Figure 11: Instantaneous iso-surface of Q colored by velocity magnitude to present boundary-layer transition on the upper surface of each wing element, red dots are transition location computed using the e^N method for $N = 7$ by Eliasson et al. [52]. (a) $Q = 2e7$; (b)$Q = 1e8$.

The FW-H sampling surface is defined as the slat surface with the transition region excluded, which prevents contamination from transition pressure fluctuations in far-field noise predictions [2]. The predicted far-field slat noise spectrum is compared with wind tunnel data from an alternative Trap Wing model [2] in Fig. 12. It should be noted that this Trap Wing model with wind tunnel acoustic data has some differences compared to the "Config 1" model. Specifically, it has a part-span flap with slat and flap deflection angles of $\delta_s = 25°$ and $\delta_f = 30°$, respectively, and a flow incidence of 10° rather than 13° [50]. According to the result from Souza et al. [5], an increase in δ_s correlates with a decrease in tonal noise frequencies and an increase in tonal noise amplitude. A higher AoA will also lead to lower tonal noise frequencies, whereas the tonal noise amplitude will reduce slightly. The combined effects of these two factors are precisely represented in Fig. 12. Regarding the broadband component, it exhibits a comparable trend to the experimental spectrum within the low to mid frequency range.

Furthermore, when comparing the far-field slat noise spectrum of the 30P30N 2.5D high-lift airfoil with

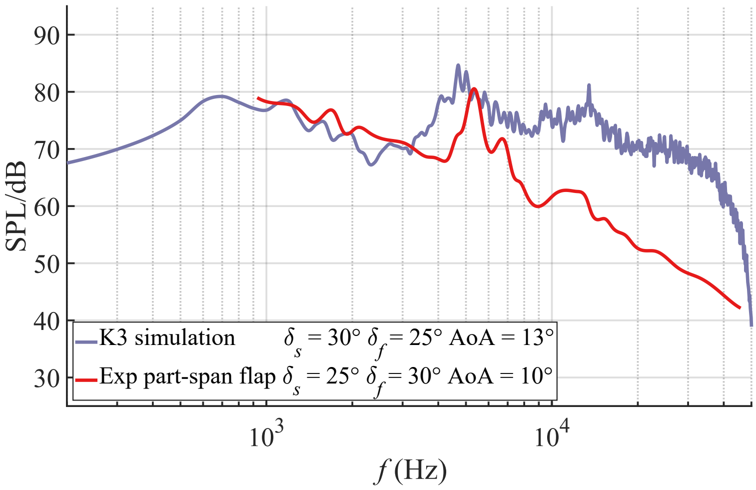

Figure 12: Trap Wing far-field slat noise spectrum compared to a NASA experiment [50] with different Trap Wing model.

that of the 3D model, it is evident that the latter exhibits fewer tonal noise frequencies. This discrepancy may be attributed to spanwise flow effects. The feedback loop of the shear layer varies across different stations. As shown in Fig. 13, notable differences in the behavior of the slat shear layer along the spanwise direction can be seen. The closer to the slat wing tip, the more evident the concentration of the cove vortex becomes.

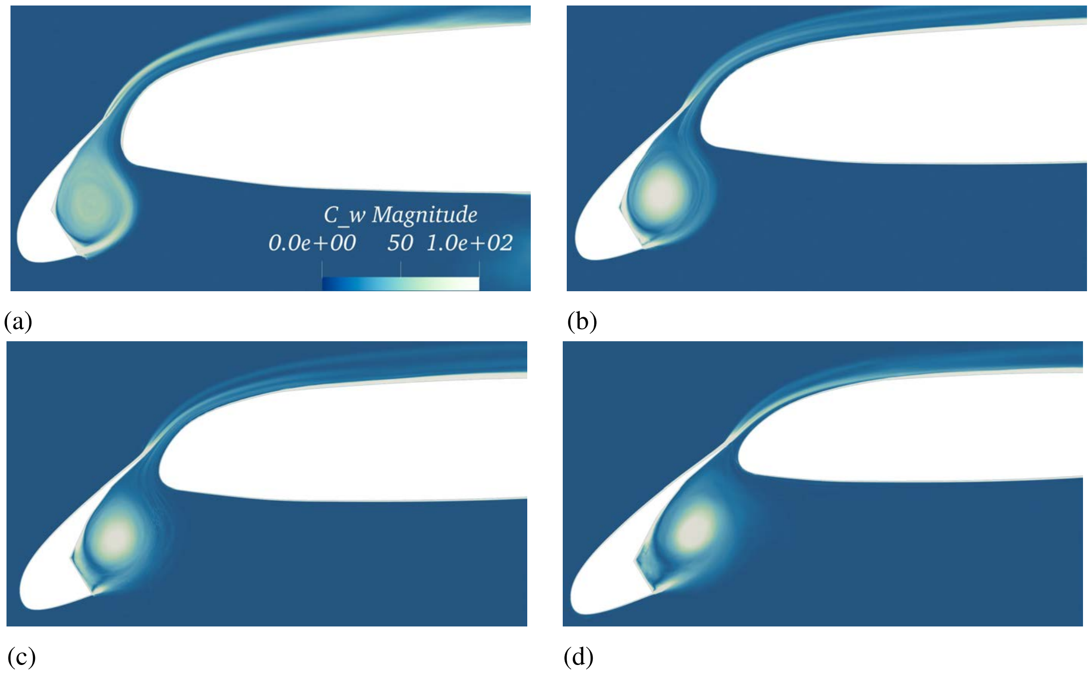

Figure 13: Contours of time-averaged normalized vorticity magnitude C_ω along spanwise station (a) η = 20%; (b) η = 45%; (c) η = 70%; (d) η = 95%.

4. Conclusions

High-order WRLES simulations are conducted for the 30P30N 2.5D high-lift airfoil and the Trap Wing semi-span 3D aircraft configuration. Comparisons of aerodynamic forces, far-field noise spectra, and flow field characteristics with experimental measurements and a traditional second-order FV solver validate the capability of DIMAXER for accurate and cost-effective noise prediction in engineering high-lift scenarios.

In terms of 30P30N high-lift airfoil slat noise, DIMAXER only requires 4 RTX 4090D GPUs to acquire K4 WRLES flow field and noise spectra that match the experimental datasets very well. In comparison, the conventional FV solver OpenCFD-EC, performing IDDES, necessitates the utilization of 3000 CPU cores, resulting in a hardware wall time that is four times greater than that of DIMAXER, while also producing a lower resolution flow field. Let alone other researchers performing WMLES on an FV solver with a 3.5 billion-cell mesh, using 55,296 CPU cores.

Subsequently, to align more closely with the actual requirements of the aviation industry, the Trap Wing model from HLPW-1 is chosen. Under K3 simulation, the computational cost for advancing 6 FPTs over 0.32 billion DoFs is limited to 8 RTX 4090D GPUs operating for less than 9 days. The aerodynamic forces and aeroacoustic results are compared to experimental data, yielding a reasonably good agreement. Additionally, the transition positions on wing element upper surfaces predicted by DIMAXER show excellent agreement with workshop data, validating transition prediction capabilities of DIMAXER.

Acknowledgments

This work is supported by the National Natural Science Foundation of China (NSFC) under grant number 12272024 and 12472298. The first author gratefully acknowledges Professor Xinliang Li from LHD, Institute of Mechanics, Chinese Academy of Sciences, for providing computational resources for OpenCFD-EC simulations.

References

[1] John E Ffowcs Williams and David L Hawkings. Sound generation by turbulence and surfaces in arbitrary motion. *Philosophical Transactions of the Royal Society of London. Series A, Mathematical and Physical Sciences*, 264(1151):321–342, 1969.

[2] Keli Zhang, Peiqing Liu, Shizhi Lin, Kai Liu, and Yi Lu. Sweep effects on slat tonal noise. *AIAA Journal*, 64(6):3399–3420, 2026.

[3] André FP Ribeiro, Mehdi R Khorrami, Ryan Ferris, Benedikt König, and Patricio A Ravetta. Lessons learned on the use of data surfaces for ffowcs williams-hawkings calculations: Airframe noise applications. *Aerospace Science and Technology*, 135:108202, 2023.

[4] Junhui Gao, Xiaodong Li, and Dakai Lin. Numerical simulation of the 30p30n high-lift airfoil noise with spectral difference method. *AIAA Journal*, 58(6):2517–2532, 2020.

[5] Daniel S Souza, Daniel Rodríguez, Fernando HT Himeno, and Marcello AF Medeiros. Dynamics of the large-scale structures and associated noise emission in airfoil slats. *Journal of Fluid Mechanics*, 875:1004–1034, 2019.

[6] Yufei Zhang, Haixin Chen, Kan Wang, and Meng Wang. Aeroacoustic prediction of a multi-element airfoil using wall-modeled large-eddy simulation. *AIAA Journal*, 55(12):4219–4233, 2017.

[7] Marc Terracol, Eric Manoha, Mitsuhiro Murayama, and Kazuomi Yamamoto. Aeroacoustic calculations of the 30p30n high-lift airfoil using hybrid rans/les methods: modeling and grid resolution effects. In *21st AIAA/CEAS Aeroacoustics Conference*, page 3132, 2015.

[8] Jeffrey P Slotnick, Abdollah Khodadoust, Juan Alonso, David Darmofal, William Gropp, Elizabeth Lurie, and Dimitri J Mavriplis. Cfd vision 2030 study: a path to revolutionary computational aerosciences. Technical report, 2014.

[9] Yang Zhang, Louis Cattafesta, Kyle Pascioni, and Meelan Choudhari. Slat noise in high-lift systems. *Progress in Aerospace Sciences*, 146:100996, 2024.

[10] Gonzalo Arranz, Yuenong Ling, Sam Costa, Konrad Goc, and Adrián Lozano-Durán. Building-block-flow computational model for large-eddy simulation of external aerodynamic applications. *Communications Engineering*, 3(1):127, 2024.

[11] ZJ Wang. High-order wall-modeled large-eddy simulation of high-lift configuration. *AIAA Journal*, 62(9):3326–3339, 2024.

[12] Malav Soni, Roland Ewert, Michael Pott-Pollenske, and Jan W Delfs. Lbm-based direct noise computation of a swept high-lift wing section with slat-track and active noise control. In *30th AIAA/CEAS Aeroacoustics Conference (2024)*, page 3060, 2024.

[13] Neil Farvolden, Ross Cruikshank, Marinus K Okoronkwo, Satoshi Baba, Hadar Ben-Gida, Philippe Lavoie, Oksana Stalnov, and Stephane Moreau. Flap side edge aeroacoustics of the 30p30n high-lift airfoil. In *30th AIAA/CEAS Aeroacoustics Conference (2024)*, page 3006, 2024.

[14] Konrad Goc, Sanjeeb T Bose, and Parviz Moin. Large eddy simulation of the nasa high-lift common research model. In *AIAA SciTech 2022 Forum*, page 1556, 2022.

[15] Bernardo Cockburn, George E Karniadakis, and Chi-Wang Shu. The development of discontinuous galerkin methods. In *Discontinuous Galerkin methods: theory, computation and applications*, pages 3–50. Springer, 2000.

[16] Yu Lv, Yee Chee See, and Matthias Ihme. An entropy-residual shock detector for solving conservation laws using high-order discontinuous galerkin methods. *Journal of Computational Physics*, 322:448–472, 2016.

[17] Yu Lv, Xiang IA Yang, George I Park, and Matthias Ihme. A discontinuous galerkin method for wall-modeled large-eddy simulations. *Computers & Fluids*, 222:104933, 2021.

[18] Hung T Huynh. A flux reconstruction approach to high-order schemes including discontinuous galerkin methods. In *18th AIAA computational fluid dynamics conference*, page 4079, 2007.

[19] Yi Lu, Teng Cao, and Kai Liu. Grid-size requirements for large eddy simulations: estimates for different orders of accuracy based on local reconstruction type schemes. In *AIAA Aviation 2019 Forum*, page 3422, 2019.

[20] Kai Liu and Yi Lu. Ultra-fast high order unsteady simulations on gpus based on a new computational model. In *AIAA Aviation 2019 Forum*, page 3525, 2019.

[21] ZJ Wang. High order wall-modeled large-eddy simulation on mixed unstructured meshes. *AIAA Journal*, 60(12):6881–6896, 2022.

[22] ZJ Wang and Avery Hantla. Towards wall-resolved large-eddy simulation of the high-lift common research model. *Journal of Aircraft*, pages 1–11, 2024.

[23] Gregor J Gassner, Florian Hindenlang, and Claus-Dieter Munz. A runge-kutta based discontinuous galerkin method with time accurate local time stepping. In *Adaptive High-Order Methods in Computational Fluid Dynamics*, pages 95–118. World Scientific, 2011.

[24] Gregor Gassner, Michael Dumbser, Florian Hindenlang, and Claus-Dieter Munz. Explicit one-step time discretizations for discontinuous galerkin and finite volume schemes based on local predictors. *Journal of Computational Physics*, 230(11):4232–4247, 2011.

[25] Yoshiaki Abe, Issei Morinaka, Takanori Haga, Taku Nonomura, Hisaichi Shibata, and Koji Miyaji. Stable, non-dissipative, and conservative flux-reconstruction schemes in split forms. *Journal of Computational Physics*, 353:193–227, 2018.

[26] Hiroyuki Asada, Seiya Sato, Naoki Miwa, and Soshi Kawai. Aeroacoustics simulations using kinetic-energy and entropy preserving (keep) schemes. In *30th AIAA/CEAS Aeroacoustics Conference (2024)*, page 3244, 2024.

[27] Philippe R Spalart. Strategies for turbulence modelling and simulations. *International journal of heat and fluid flow*, 21(3):252–263, 2000.

[28] Philippe R Spalart and V Venkatakrishnan. On the role and challenges of cfd in the aerospace industry. *The Aeronautical Journal*, 120(1223):209–232, 2016.

[29] Xinliang Li, Dexun Fu, and Yanwen Ma. Direct numerical simulation of hypersonic boundary layer transition over a blunt cone with a small angle of attack. *Physics of Fluids*, 22(2), 2010.

[30] Aude Bernard-Champmartin and Florian De Vuyst. A low diffusive lagrange-remap scheme for the simulation of violent air–water free-surface flows. *Journal of Computational Physics*, 274:19–49, 2014.

[31] Minwoo Kim, Jiseop Lim, Seungtae Kim, Solkeun Jee, and Donghun Park. Assessment of the wall-

adapting local eddy-viscosity model in transitional boundary layer. *Computer Methods in Applied Mechanics and Engineering*, 371:113287, 2020.

[32] Eleuterio F Toro. *Riemann solvers and numerical methods for fluid dynamics: a practical introduction*. Springer Science & Business Media, 2009.

[33] Lin Mu, Junping Wang, Yanqiu Wang, and Xiu Ye. Interior penalty discontinuous galerkin method on very general polygonal and polyhedral meshes. *Journal of computational and applied mathematics*, 255:432–440, 2014.

[34] William John Feiereisen. *Numerical simulation of a compressible, homogeneous, turbulent shear flow*. Stanford University, 1981.

[35] Brynjulf Owren and Marino Zennaro. Derivation of efficient, continuous, explicit runge–kutta methods. *SIAM journal on scientific and statistical computing*, 13(6):1488–1501, 1992.

[36] Keli Zhang, Changping Yu, Peiqing Liu, and Xinliang Li. An mpi-openmp mixing parallel open source fw-h code for aeroacoustics calculation, 2023.

[37] Meelan M Choudhari and David P Lockard. Assessment of slat noise predictions for 30p30n high-lift configuration from banc-iii workshop. In *21st AIAA/CEAS aeroacoustics conference*, page 2844, 2015.

[38] Mitsuhiro Murayama, Kazuyuki Nakakita, Kazuomi Yamamoto, Hiroki Ura, Yasushi Ito, and Meelan M Choudhari. Experimental study on slat noise from 30p30n three-element high-lift airfoil at jaxa hard-wall lowspeed wind tunnel. In *20th AIAA/CEAS aeroacoustics conference*, page 2080, 2014.

[39] Mitsuhiro Murayama, Yuzuru Yokokawa, Hiroki Ura, Kazuyuki Nakakita, Kazuomi Yamamoto, Yasushi Ito, Takehisa Takaishi, Ryotaro Sakai, Keiji Shimoda, Takayuki Kato, et al. Experimental study of slat noise from 30p30n three-element high-lift airfoil in jaxa kevlar-wall low-speed wind tunnel. In *2018 AIAA/CEAS Aeroacoustics Conference*, page 3460, 2018.

[40] Kyle Pascioni, Louis N Cattafesta, and Meelan M Choudhari. An experimental investigation of the 30p30n multi-element high-lift airfoil. In *20th AIAA/CEAS aeroacoustics conference*, page 3062, 2014.

[41] Kyle A Pascioni and Louis N Cattafesta. Aeroacoustic measurements of leading-edge slat noise. In *22nd AIAA/CEAS aeroacoustics conference*, page 2960, 2016.

[42] Keli Zhang, Shizhi Lin, Peiqing Liu, Zhibo Zhang, Shihao Liu, Can Fang, Kai Liu, Yi Lu, and Yu Lv. Cfd-based aerodynamic and aeroacoustic optimization of the 30p30n high-lift airfoil. In *32nd AIAA/CEAS Aeroacoustics Conference (2026)*, page 3256, 2026.

[43] Keli Zhang, Shizhi Lin, Peiqing Liu, Shihao Liu, Yuping Ren, Kai Liu, Yi Lu, and Yu Lv. Aeroacoustic control of slat noise: Dependence of noise reduction on angle-of-attack using a novel staggered serration design. In *32nd AIAA/CEAS Aeroacoustics Conference (2026)*, page 3208, 2026.

[44] Guoyong Chen, Xiaolong Tang, Xiaoquan Yang, Peifen Weng, and Jue Ding. Noise control for high-lift devices by slat wall treatment. *Aerospace Science and Technology*, 115:106820, 2021.

[45] Kazuomi Yamamoto, Mitsuhiro Murayama, Kazuhide Isotani, Yosuke Ueno, Kensuke Hayashi, and Tohru Hirai. Slat noise reduction based on turbulence attenuation downstream of shear-layer reattachment. In *28th AIAA/CEAS Aeroacoustics 2022 Conference*, page 2954, 2022.

[46] Keli Zhang, Zhibo Zhang, Shizhi Lin, Peiqing Liu, and Shihao Liu. Multiple deep learning surrogate models for aeroacoustic prediction of the 30p30n high-lift airfoil. In *32nd AIAA/CEAS Aeroacoustics Conference (2026)*, page 3450, 2026.

[47] Nicholas J Georgiadis, Donald P Rizzetta, and Christer Fureby. Large-eddy simulation: current capabilities, recommended practices, and future research. *AIAA journal*, 48(8):1772–1784, 2010.

[48] Eric Manoha and Bastien Caruelle. Summary of the lagoon solutions from the benchmark problems for airframe noise computations-iii workshop. In *21st AIAA/CEAS aeroacoustics conference*, page 2846, 2015.

[49] Christopher L Rumsey, Jeffrey P Slotnick, Michael Long, Robert A Stuever, and TR Wayman. Summary of the first aiaa cfd high-lift prediction workshop. *Journal of Aircraft*, 48(6):2068–2079, 2011.

[50] Craig Streett, Jay Casper, David Lockard, Mehdi Khorrami, Robert Stoker, Ronen Elkoby, Wayne Wenneman, James Underbrink, Wayne Wenneman, and James Underbrink. Aerodynamic noise reduction for high-lift devices on a swept wing model. In *44th AIAA aerospace sciences meeting and exhibit*, page 212, 2006.

[51] Tony Sclafani, Jeffrey Slotnick, John Vassberg, Thomas Pulliam, and Henry Lee. Overflow analysis of the nasa trap wing model from the first high lift prediction workshop. In *49th AIAA Aerospace Sciences Meeting including the New Horizons Forum and Aerospace Exposition*, page 866, 2011.

[52] Peter Eliasson, Ardeshir Hanifi, and Shia-Hui Peng. Influence of transition on high-lift prediction with the nasa trap wing model. In *29th AIAA Applied Aerodynamics Conference*, page 3009, 2011.

[53] Adam M Clark, Jeffrey P Slotnick, Nigel J Taylor, and Christopher L Rumsey. Requirements and challenges for cfd validation within the high-lift common research model ecosystem. In *AIAA Aviation 2020 Forum*, page 2772, 2020.